

pubs.acs.org/JACS Article

Co-Cu Bimetallic Metal Organic Framework Catalyst Outperforms the Pt/C Benchmark for Oxygen Reduction

Mohamed Fathi Sanad, Alain R. Puente Santiago, Sarah A. Tolba, Md Ariful Ahsan, Olivia Fernandez-Delgado, Mina Shawky Adly, Elhussein M. Hashem, Mohamed Mahrous Abodouh, M. Samy El-Shall, Sreeprasad T. Sreenivasan, Nageh K. Allam, and Luis Echegoyen



Cite This: J. Am. Chem. Soc. 2021, 143, 4064-4073



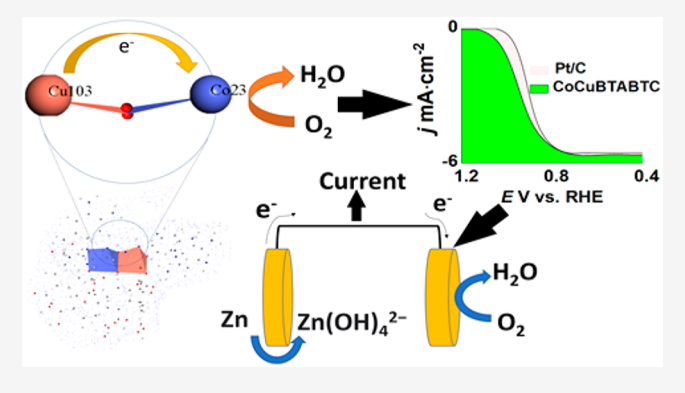
ACCESS

Metrics & More

Article Recommendations

s) Supporting Information

ABSTRACT: Platinum (Pt)-based-nanomaterials are currently the most successful catalysts for the oxygen reduction reaction (ORR) in electrochemical energy conversion devices such as fuel cells and metal-air batteries. Nonetheless, Pt catalysts have serious drawbacks, including low abundance in nature, sluggish kinetics, and very high costs, which limit their practical applications. Herein, we report the first rationally designed nonprecious Co–Cu bimetallic metal—organic framework (MOF) using a low-temperature hydrothermal method that outperforms the electrocatalytic activity of Pt/C for ORR in alkaline environments. The MOF catalyst surpassed the ORR performance of Pt/C, exhibiting an onset potential of 1.06 V vs RHE, a half-wave potential of 0.95 V vs RHE, and a higher electrochemical stability ($\Delta E_{1/2} = 30$ mV) after



1000 ORR cycles in 0.1 M NaOH. Additionally, it outperformed Pt/C in terms of power density and cyclability in zinc-air batteries. This outstanding behavior was attributed to the unique electronic synergy of the Co–Cu bimetallic centers in the MOF network, which was revealed by XPS and PDOS.

INTRODUCTION

The engineering of self-assembled supramolecular coordination metal complexes to fabricate inexpensive catalytic systems with ultrahigh intrinsic activities is changing the landscape in the race to find a "Holy Grail" catalyst for high-powered electrochemical energy conversion devices. 1-3 The tailoring of the interactions between metal catalytic centers and organic linkers in supramolecular systems that contain earth-abundant elements is currently opening new horizons for the rational design of new oxygen reduction catalysts.^{4,5} These properties can outperform and lead to the replacement of Pt-based catalysts in practical advanced energy systems such as fuel cells and metal-air batteries. Recently, metal organic frameworks (MOF)-based materials have emerged as a new class of successful supramolecular non-noble materials for oxygen reduction reactions (ORR) due to the organic ligands/metal atom interactions that provide highly tunable porous interconnected frameworks, high surface areas, and fully exposed and well-dispersed metallic centers for electrocatalysis; thus they overcome the typical kinetic issues of Pt catalysts in fuel cells, such as mass transport and multielectron transfer. 6-10 It is well-known that the electronic properties of catalytic materials dictate the interactions between the reactants and intermediate species with the catalyst surfaces as well as the catalytic yields. 11 The addition of extra metals

into the inorganic/organic network was explored to improve the electrocatalytic properties of MOF materials, since synergistic bimetallic systems can drastically decrease the energy barriers between the intermediate species of the ORR reaction. 12–14 For instance, lattice-strained bimetallic FeNi MOFs have shown impressive bifunctional activity for oxygen electrocatalysis, exhibiting the desired preference for the 4-electron kinetic pathway. The organometallic structures offer various unexplored avenues to tune the synergistic electronic interactions of the bimetallic centers and, consequently, the overall catalytic activity.

Herein, we report a Co–Cu MOF architecture synthesized via low-temperature hydrothermal strategy using 1,2,4,5 benzene tetraamine (BTA) and benzene-1,3,5-tricarboxylic acid (BTC). The catalytic activity of the MOF structures was tuned by varying the Co/Cu molar ratios. The optimized Co/Cu (1:1) structure (named as BTC-Co-O-Cu-BTA) exhibited unique structural properties such as well-interconnected O-

Received: February 1, 2021 Published: March 4, 2021





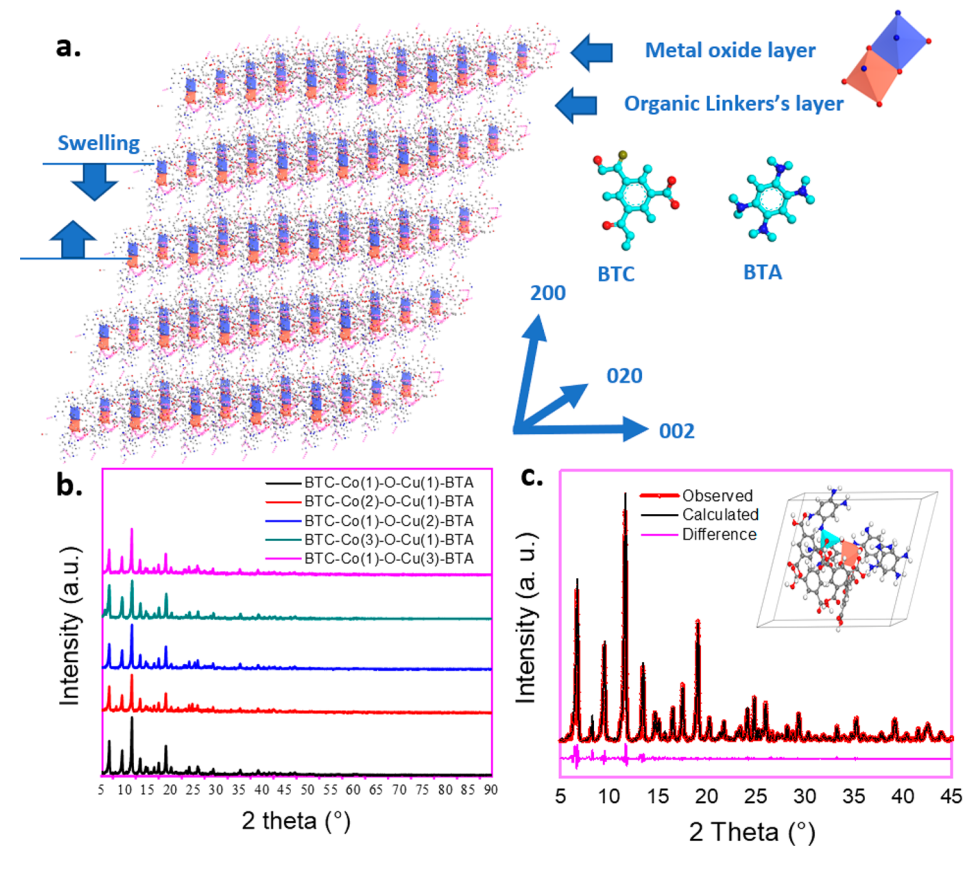


Figure 1. (a) Representation of the BTC-Co-O-Cu-BTA simulated structure, metal octahedral centers and organic linkers. (b) X-ray diffraction pattern of BTC-Co-O-Cu-BTA MOF with different Co/Cu molar ratios. (c) Fitted X-ray powder diffraction spectrum of BTC-Co-O-Cu-BTA MOF and the corresponding simulated XRD (inset: the obtained structure).

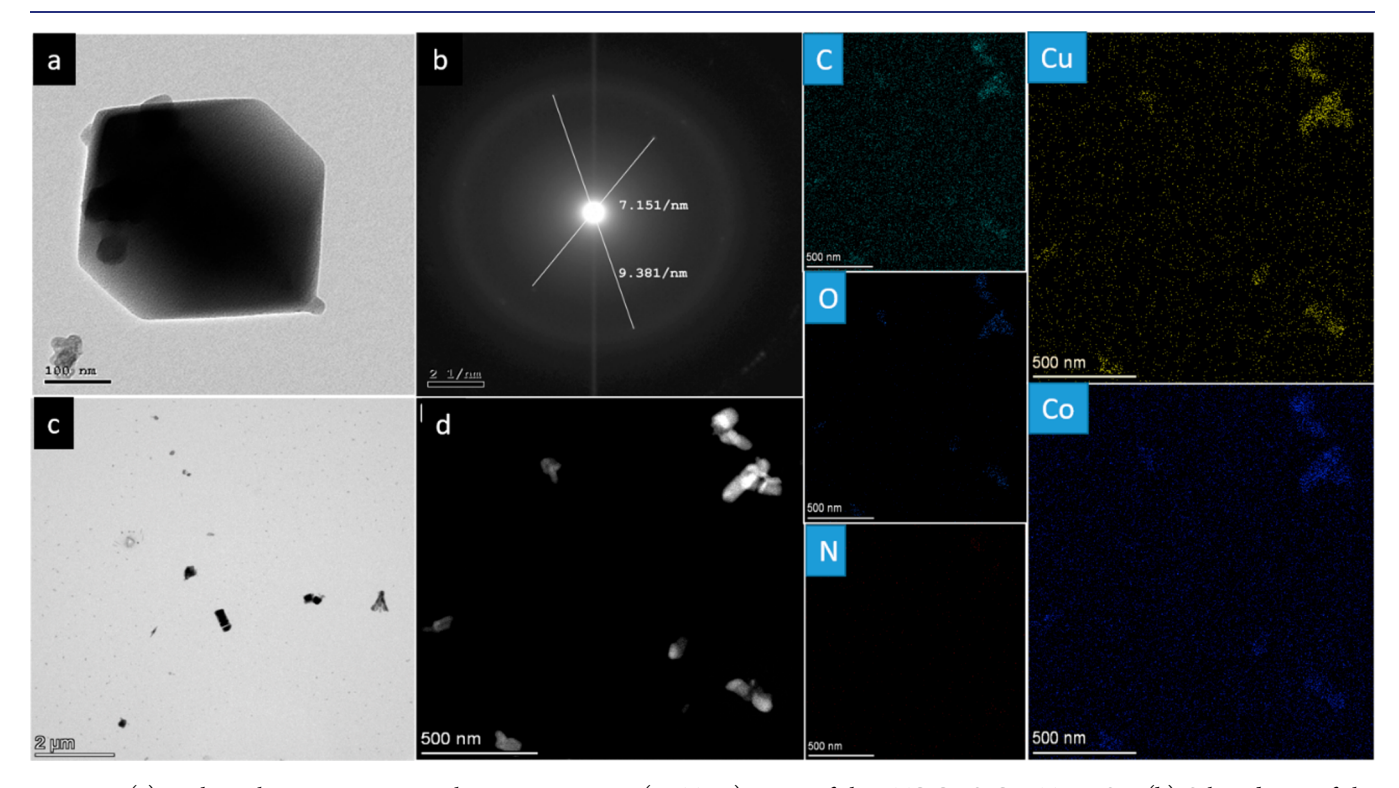


Figure 2. (a) High-resolution transmission electron microscopy (HRTEM) image of the BTC-Co-O-Cu-BTA MOF. (b) Selected area of the electron diffraction pattern. (c) TEM and (d) STEM of the BTC-Co-O-Cu-BTA MOF and corresponding EDS mapping.

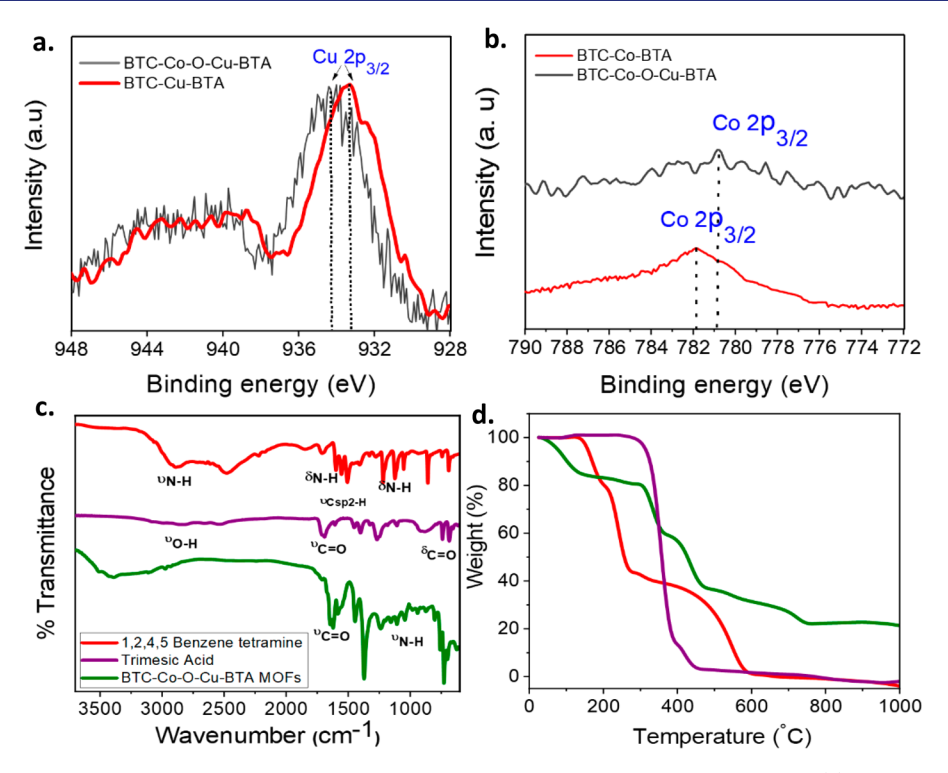


Figure 3. (a) and (b) XPS spectra of Cu $2p_{3/2}$ and Co $2p_{3/2}$ in bimetallic and monometallic form, respectively. (c) FTIR spectra of the as-prepared BTC-Co-O-Cu-BTA MOF and 2 organic linkers. (d) TGA spectra of the BTC-Co-O-Cu-BTA MOF and 2 organic linkers.

bridged Co–Cu bimetallic centers, which were fully characterized with multiple techniques. The BTC-Co-O-Cu-BTA MOF surpassed the Pt/C catalytic performance showing impressive onset and half-wave potential values of 1.06 and 0.95 V vs RHE, respectively, resulting in the best nonprecious ORR catalyst to date. Co–Cu MOF also exceeded the performance of Pt/C in zinc-air batteries. XPS analysis and DFT calculations demonstrated that the strong electronic coupling between Co and Cu triggered an effective interatomic electron transfer process, which is the key factor for the generation of very efficient catalytic ORR centers.

■ RESULTS AND DISCUSSION

Structural Characterization. The bimetallic BTC-Co-O-Cu-BTA MOF materials were prepared by coordinating Co²⁺ and Cu²⁺ ions using BTC and BTA as organic linkers via a lowtemperature hydrothermal method. Ligands and MOF structure are presented in Figure 1a, together with the interlayer spacing. The reaction proceeded by an initial nucleation of small MOF crystals and the self-assembly of Obridged Co and Cu clusters. Figure 1b displays the X-ray diffraction (XRD) patterns for the bimetallic BTC-Co-O-Cu-BTA MOF with different Co/Cu molar ratios. In these structures, both the Co and Cu atoms are octahedrally coordinated by six oxygen atoms in the MOF framework. Furthermore, these pseudo octahedra exhibit many edge/ corner centers connected along the direction of the crystallographic plane to form 3D bimetal layers separated by BTA and BTC organic linkers. Figure 1c shows the experimental and simulated XRD patterns as well as the differences for the BTC-Co-O-Cu-BTA MOF with a 97% match percentage. This BTC-Co-O-Cu-BTA MOF structure is composed of BTA, BTC ligands, and Co, Cu octahedral centers with (1:1) molar ratios. The edge/corner-rich structure increases the number of effective catalytic sites, while the MOF network allows ion accessibility, thus enhancing the mass transport along the bimetallic MOF material and, in turn, the electrocatalytic yields.

The structural and morphological properties of the BTC-Co-O-Cu-BTA MOF crystals revealed cuboid structures (triclinic morphology) with a size close to 500 nm, as determined by high-resolution transmission electron microscopy (HRTEM); Figure 2a.¹⁷ The Co-Cu MOF lattice fringe is 7.15 nm, which can be ascribed to an interlayer-spacing of the MOF with transition metal nodes along the [200] crystallographic direction (Figure 2a-c). Electron mapping confirmed a well-dispersed distribution of Co and Cu metal ions throughout the MOF framework (Figure 2d). To investigate the electronic properties of the BTC-Co-O-Cu-BTA MOF, X-ray photoelectron spectroscopy (XPS) measurements were recorded (Figure 3a,b). The high-resolution spectrum of Cu 2p reveals a peak at 934.21 eV, which is related to Cu-O bonds in the bimetallic systems. Interestingly, this peak was shifted from 932.1 to 933.21 eV when the MOF structure changed from monometallic to bimetallic. The peak of Co 2p at 779.5 eV in the bimetallic MOF can be attributed to the inherent character of high spin Co²⁺ in the Co-linker (Figure 3b). In contrast, the Co 2p for the monometallic cobalt MOF was observed at 781.5 eV. The observed shifts for both metals resulting from the bimetallic interaction can be explained by electron-density migration from Cu to Co via the O-bridges. 18,19 The HR-XPS of other elements (C, O and N) were also studied (SI Figure 1a-d). Fourier-transform infrared spectroscopy (FTIR) was employed to obtain a deeper insight about the structural properties of the BTC-Co-O-Cu-BTA MOF. A detailed analysis of the vibrational modes of the two starting organic linkers and the BTC-Co-O-Cu-BTA MOF was performed. As can be seen in Figure 3c, benzene-1,3,5-

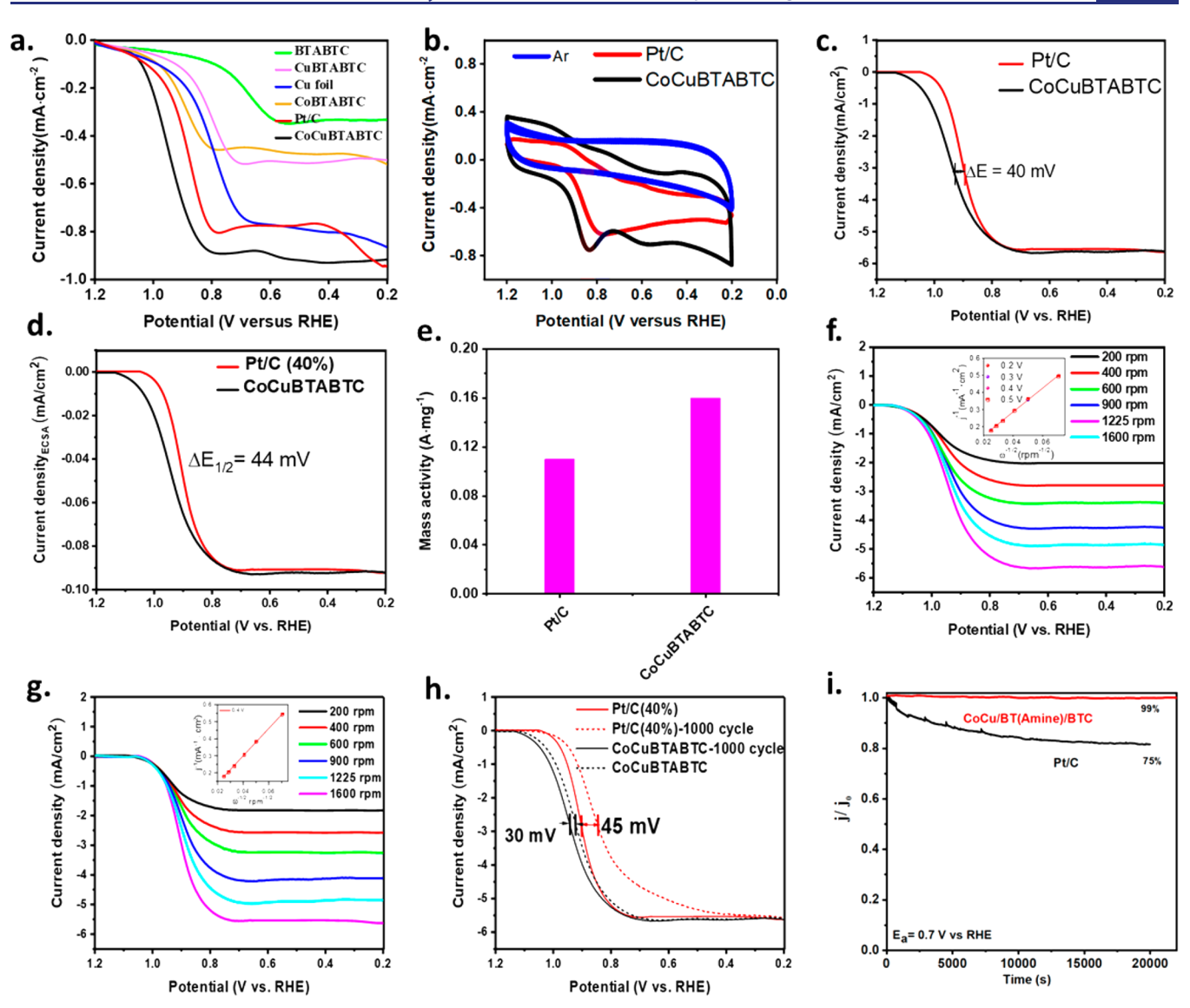


Figure 4. Oxygen reduction electrocatalytic performance in an O_2 -saturated NaOH solution. (a) Linear sweep voltammetry of the BTC-Co-O-Cu-BTA MOF, monometallic MOFs, Cu foil and Pt/C (electrode-rotating speed, 0 r.p.m; scan rate: 2 mV s⁻¹); (b) CV profiles recorded for BTC-Co-O-Cu-BTA MOF and Pt/C in N₂- (dotted) and O_2 -saturated (solid) 0.1 M NaOH solution; (c) LSVs for BTC-Co-O-Cu-BTA and Pt/C (electrode-rotating speed, 1600 r.p.m; loading: 50 μg·cm⁻²; scan rate: 10 mV s⁻¹); (d) ECSA normalized LSV for both BTC-Co-O-Cu-BTA MOF and Pt/C; (e) mass activity of both BTC-Co-O-Cu-BTA MOF and Pt/C at 0.90 V vs RHE. (f) The rotating disk electrode plots of the Co-Cu MOF in oxygen-saturated 0.1 M NaOH at rotation speeds ranging from 200 to 1600 r.p.m and a scan rate of 10 mV s⁻¹; inset (Koutecky-Levich (K-L) curves); (g) Rotating disk electrode plots of Pt/C in oxygen-saturated 0.1 M NaOH at rotation speeds ranging from 200 to 1600 r.p.m and a scan rate of 10 mV s⁻¹; inset (K-L plots); (h) polarization curves of BTC-Co-O-Cu-BTA MOF and Pt/C catalysts before (solid) and after (dotted) the durability tests. (i) I-t curve for BTC-Co-O-Cu-BTA MOF and its comparison with commercial Pt/C at 0.70 V vs RHE.

tricarboxylic acid shows typical O–H stretching modes around 3340 cm⁻¹ and carbonyl stretching at 1723–1689 cm⁻¹, while 1,2,4,5-tetraaminobenzene tetrahydrochloride exhibits typical N–H stretching modes at 3031–2798 cm⁻¹, N–H and C–H bending modes at 1609 and 1503 cm⁻¹, as well as C–N stretching at 1220 cm⁻¹. Comparing the FTIR spectra of the BTC-Co-O-Cu-BTA MOF to those of the corresponding starting materials, some differences can be observed. In the case of the newly synthesized MOFs, the carbonyl group stretching is shifted toward higher frequencies (1653, 1619 cm⁻¹), a clear indication of coordination of the carboxylic acid groups with Cu and Co. Similarly, the C–N stretching shifts to 1103 cm⁻¹, demonstrating a similar interaction or coordination of the amine groups with the metals.¹⁹ For a better understanding of the structural features of the BTC-Co-O-

Cu-BTA MOF, thermogravimetric measurements (TGA) were conducted. The TGA profiles of the benzene-1,3,5-tricarboxylic acid, 1,2,4,5-tetraaminobenzene tetrahydrochloride, and the Co–Cu MOF are shown in Figure 3d. The TGA study revealed that in the case of the MOF, 15% of the initial mass is lost at temperatures as low as 60 °C, which could correspond to the loss of the amino groups. Next, 25% of the mass is lost at 306 °C and 23% at 367 °C, which, based on the information obtained from the TGA profiles of the starting materials, could correspond to the loss of the benzene-1,3,5-tricarboxylic acid fragments. Two additional losses of 9% and 7% occur at 473 and 613 °C, which could correspond to the loss of the benzene rings, leaving a remaining 21% of the mass that corresponds to the metals in the structure. A detailed analysis of each compound was conducted (SI Figure 2). The Brunauer—

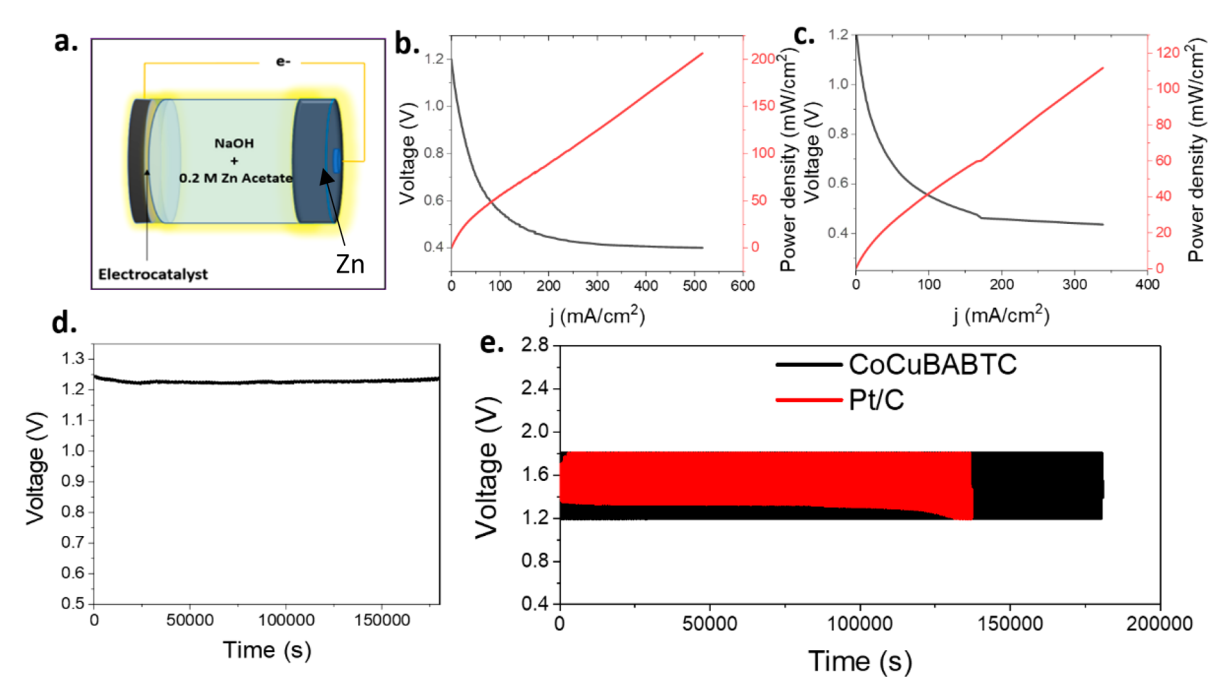


Figure 5. Zinc air battery application using Zn foil and Zinc acetate as the electrolyte over both BTC-Co-O-Cu-BTA MOF and Pt/C cathodes. (a) Zinc air battery design; (b and c) the corresponding calculated power densities in mW for Co-Cu MOF and Pt/C; (d) discharge curve for the BTC-Co-O-Cu-BTA MOF; (e) charge and discharge cycling curves of Zn-air batteries and Pt/C at current density of 50 mA·cm⁻².

Emmett—Teller (BET) technique was used to determine the specific surface areas (S_BET) of the BTC-Co-O-Cu-BTA MOFs, which were found to be 308.8 m²/g, with an average pore width of 137.4 Å (SI Figure 3).

Electrocatalytic Activity and Stability. The electrocatalytic properties of the bimetallic BTC-Co-O-Cu-BTA MOF were extensively investigated by different electrochemical techniques in NaOH solution. The influence of the Co/Cu ratio on the oxygen electroreduction behavior was examined under non dynamic electrochemical conditions using linear sweep voltammetry (LSV). The BTC-Co-O-Cu-BTA MOF electrocatalysts substantially surpass the electrocatalytic activity of other monometallic and bimetallic MOF materials as well as that for the Pt/C benchmark catalyst at 0 rpm (Figure 4a, SI Figure 4). This indicates that the well-dispersed Obridged bimetallic Co-Cu centers and the highly porous interconnected 3D framework dramatically improve the electrocatalytic rates for oxygen reduction. The shift of the onset potential values as a function of the Co/Cu ratios (SI Figure 4a,b) can be ascribed to the supramolecular metallic interactions. These interactions promote significant differences in the crystalline MOF network as well as in the local electronic structure of the Co-Cu catalytic sites, thus lowering the energy barriers for intermediate catalytic species and increasing the ORR catalytic activity. Furthermore, a welldefined cathodic peak of the BTC-Co-O-Cu-BTA MOF CV in O₂-saturated conditions is observed at ≈0.84 V vs RHE, which substantially outperforms that of the Pt/C oxygen electroreduction peak by around 50 mV (Figure 4b). The ORR performance was also investigated under a nitrogen atmosphere and for a clean free glassy carbon electrode as control, which shows very low activity as shown in (SI Figure 5).

The electrocatalytic performance of the optimized BTC-Co-O-Cu-BTA MOF catalysts was further compared with that of the Pt/C benchmark at a rotational speed of 1600 rpm and a scan rate of $10~\text{mV}\cdot\text{s}^{-1}$ following the US Department of Energy

protocol (Figure 4c). ²³ Remarkably, the catalyst outperformed the catalytic performance of commercial Pt/C, exhibiting an onset potential of 1.06 V vs RHE and a half-wave potential of 0.95 V vs RHE, which are 60 mV and 44 mV higher than those observed for Pt/C, respectively. To the best of our knowledge, these are the best ORR values observed to date for nonprecious catalytic systems (Table S1). Figure 4d shows the ECSA normalized LSV for both the BTC-Co-O-Cu-BTA MOF and Pt/C, which demonstrates the larger intrinsic activity of MOF material.

The mass activity value obtained from the ORR polarization curve of the BTC-Co-O-Cu-BTA MOF at 0.90 V also outperformed that of Pt/C (Figure 4e). While the Pt/C benchmark could only reach a value of 0.11 A·mg⁻¹, ²⁴ our best electrocatalytic MOF achieved a value of 0.16 A·mg⁻¹. The dynamic ORR properties at different rotation rates for both the BTC-Co-O-Cu-BTA MOF and Pt/C at a loading of 50 μ g·cm⁻² were studied in detail; this was accomplished with a rotating disk electrode (RDE) setup to probe the kinetics of the interfacial redox reactions on both catalytic surfaces under nondiffusion limited-conditions (Figure 4f,g). The rotating disk electrode system and electrode design is shown in (SI Figure 6).

The number of electrons (n) transferred to each oxygen molecule during the electrocatalytic reaction is a fundamental descriptor of the ORR kinetic efficiency. A full 4-electron reductive process to OH⁻ indicates that the reaction does not generate undesirable intermediate catalytic species such as hydrogen peroxide. The linearity of the Koutecky–Levich (K-L) plots for both materials (Figure 4f,g inset) implies a first-order reaction kinetics with respect to the concentration of dissolved oxygen. The kinetic parameters obtained from (K-L) plots demonstrated that the supramolecular material exhibits a superior catalytic activity than Pt/C under dynamic conditions. For instance, the average value of n was estimated to be 3.90 for the Co–Cu (1:1) bimetallic MOF in the

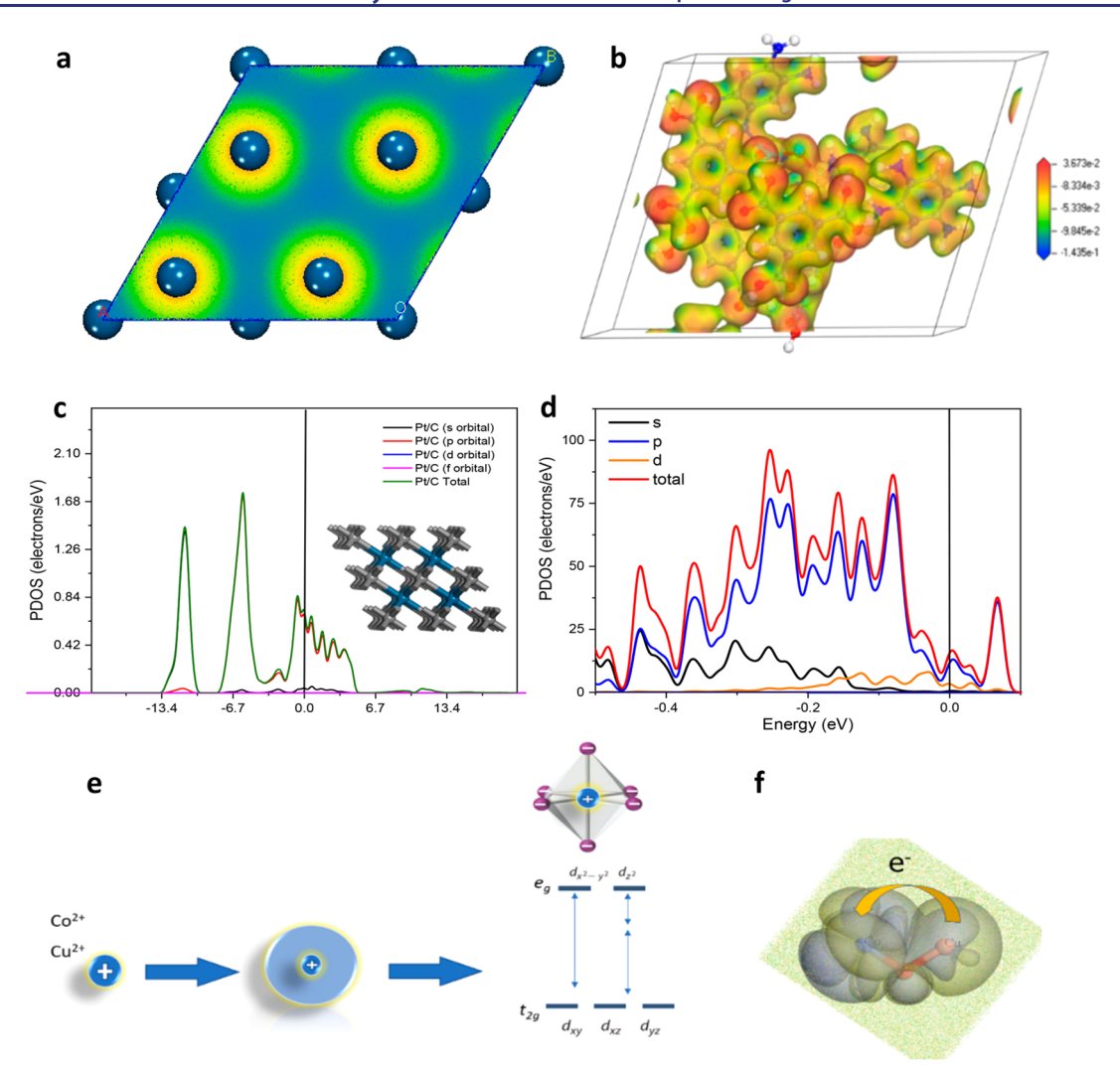


Figure 6. DFT calculations. The electron density distribution of (a) Pt/C and (b) BTC-Co-O-Cu-BTA MOF. The density of states of (c) Pt/C and (d) BTC-Co-O-Cu-BTA MOF. (e) Octahedral order of six negative charges around a metal ion complex. (f) Charge transfer direction in the Co-Cu bimetallic MOF catalyst.

potential range 0.20-0.70 V vs RHE, which is slightly higher than the value obtained for Pt/C at the same potential window (3.80). It is worth noting that the MOF exhibits a 4-electron mechanism over a large potential window of 500 mV, thus showing improved kinetic efficiencies when compared to the benchmark Pt/C catalysts. The long-term durability of the BTC-Co-O-Cu-BTA MOF and Pt/C were also assessed. Remarkably, the half-wave potential $(E_{1/2})$ for BTC-Co-O-Cu-BTA after 1 K cycles exhibited a lower shift (30 mV) compared to the value observed for commercial Pt/C (45 mV). (Figure 4h). The chronoamperometric stability responses of the BTC-Co-O-Cu-BTA MOF and Pt/C were also compared at 0.70 V vs RHE under alkaline conditions and they displayed a current drop of 1% and 25% after 20000 s, respectively, again showing the superiority of the former (Figure 4i). Table S2 summarizes the electrochemical active surface area and double-layer capacitance (C_{dl}) values of both Pt/C and BTC-Co-O-Cu-BTA MOF, which further support the higher intrinsic catalytic activity of the MOF for ORR (SI Figures 7 and 8).

Evaluation of Zn-Air Battery Performance. To compare the performance of the BTC-Co-O-Cu-BTA MOF with Pt/C as a cathode material for zinc-air battery applications, we

carefully designed a specific battery cell (Figure 5a, SI Figure 9). It is worth noting that the system was tested under normal conditions using atmospheric air instead of oxygen. To our surprise, the BTC-Co-O-Cu-BTA MOF catalyst displays a discharge and charge voltage of 1.2 V at a current density of 50 mA cm⁻², similar to the discharge voltage of Pt/C (1.15 V) at the same current density, respectively (Figure 5b,c). The calculated power densities for both BTC-Co-O-Cu-BTA and Pt/C are 200 and 110 mW/cm², respectively.²⁷ More remarkably, only small changes in the voltages were observed after 50 charge and discharge cycles. In contrast, the discharge voltage for Pt was markedly reduced after ten cycles, thus confirming the superior stability of the Co-Cu MOF (Figure 5d,e).

Mechanistic Insights of the Electrocatalytic Processes. The optimized structure and the experimental versus simulated XRD patterns are shown in Figure 1c. The surface electronic properties of catalytic systems control the reactant's binding energy as well as their electrocatalytic activities. To gain deeper insights into the ORR catalytic activity of the Co–Cu MOF, we calculated the partial electron density of states (PDOS) around the Fermi level of the modeled structure and compared them to that of Pt/C (Figure 6a,b). The PDOS

study concluded that the electron charge density is highly distributed over the Co–Cu MOF structure, ^{29–31} thus providing more active sites for ORR electrocatalysis than Pt/C. The density of states for the Co–Cu MOF is 11.4 electrons/eV near the Fermi level, which mainly consists of porbital (8.54 electrons/eV) and d-orbital electrons (2.5 electrons/eV). For Pt/C, there are only 1.9 and 0.7 electrons/eV at the Fermi level, ³² respectively (Figure 6c,d).

The PDOS study of the Co and Cu atoms in the MOF skeleton revealed a remarkably high electron density of states. Such electron density decreases the oxygen adsorption energy states of the ORR intermediate catalytic species leading to superior catalytic performances for the BTC-Co-O-Cu-BTA MOF.

Another interesting aspect is how Cu combines with Co in the BTC-Co-O-Cu-BTA framework to yield outstanding electrocatalytic activities. ^{33–35} After the formation of an octahedral metal-oxygen structure, the negative charge is then uniformly distributed in a spherical shape around the Co and Cu metal ions, splitting the d orbitals into two new states with different energies (Figure 6e). XPS analysis (Figure 2a,b) shows that the Cu²⁺ 2p_{3/2} (932.1 eV for Cu-BTABTCs) and Co²⁺ 2p_{3/2} (781.7 eV for Co-BTABTCs) peaks shift to higher and lower binding energies (Cu 2p_{3/2} and Co 2p_{3/2} of BTC-Co-O-Cu-BTA are 934.1 and 797.5 eV), respectively. This phenomenon indicates an electron transfer process from Cu²⁺ to Co²⁺ through the bridged oxygen (Figure 6f).^{36,37} The electronic (valence) configuration of Co²⁺ is 3d⁷ in a high-spin state, so Co^{2+} has unpaired electrons in the t_{2g} d-orbitals, which can interact with $O^{\bar{2}-}$ (bridged) via π -donation, while the π symmetry (t_{2g}) d-orbitals of Cu²⁺ are completely occupied,³⁸ which greatly facilitates the electron transfer in the Co-O-Cu junction. The significant repulsion between the O2- and Cu2+ and the attractive Co-O interactions can induce the interatomic electron transfer. Therefore, the change in the PDOS (SI Figure 10) of the unfilled metal 3d eg-orbitals of both Co and Cu -O bond increases and decreases, respectively, upon the bimetallic electronic coupling in the MOF network, which gives rise to a high electron localization around the Co centers, thus providing ultra-active catalytic sites for ORR electrocatalysis. To verify this conclusion, we performed density functional theory calculations to fully investigate the catalytic mechanism. Initially, adsorption energy calculations were carried out to elucidate the potential active sites for oxygen evolution. The adsorption energy of an adsorbate is calculated as $E_{ads} = E_{MOF+adsorbate} - E_{MOF} - E_{adsorbate}$ where E_{MOF+adsorbate}, E_{MOF}, and E_{adsorbate} are the total energies of the MOF molecule model and adsorbate, MOF, and a gas phase adsorbate, respectively. As seen in Table 1, O2 adsorbates exhibit less negative Eads on Co sites than on Cu sites, indicating a stable exothermic reaction with Co sites being the most probable active sites for the ORR, in excellent agreement with the calculated electronic properties of the MOF. The

Table 1. Calculated Adsorption Energies of OH and O₂ and Formation Energies of OOH and O on Co and Cu Sites

	Adsorption Energy (EV)		(B) Species	Formation Energy (EV)	
(A) Adsorbates	on Co	on Cu		on Co	on Cu
ОН	-1.125	-1.129	ООН	-2.45	-2.17
O_2	-0.394	-0.192	O	0.36	0.62

Gibbs free energy change (ΔG) at 298.15 K of the proposed ORR steps on Co sites is shown in (SI Figure 11). The low adsorption energy of O₂ on Co sites resulted in a formation energy of -2.45 eV for *OOH as shown in Table 1. Also, the small ΔG_1 of 0.433 eV facilitates a fast O₂/ $O\dot{H}$ exchange to produce (O_2) radical species that are further protonated by H₂O molecule to *OOH with ΔG_2 of 1.23 eV along with the oxidation of Co²⁺ to form a Co³⁺-OOH intermediate. Finally, the O-O bond is broken and the original state of Co³⁺ OH is recovered with free energies of -0.17 (ΔG_3) and 0.28 (ΔG_4) eV, respectively.

CONCLUSIONS

pubs.acs.org/JACS

We synthesized a new class of bimetallic Co-Cu MOFs following a one-pot low-temperature hydrothermal strategy. The catalytic properties of the nonprecious bimetallic MOF were finely tailored by varying the Co/Cu molar ratios during the synthetic reaction. The optimized Co/Cu (1:1) MOF electronic structure formed by well-dispersed O-bridged bimetallic clusters, which are interconnected into a highly porous network, led to an unique and very efficient ORR catalyst. The BTC-Co-O-Cu-BTA surpassed the ORR catalytic activity of Pt/C in terms of onset potential, half-wave potential, and electrochemical stability, thus performing as the best nonprecious ORR catalyst reported to date. The BTC-Co-O-Cu-BTA MOF also acted as an excellent cathode alternative to Pt/C in zinc-air batteries. The impressive catalytic performance was rationalized in terms of the effective interatomic Co-Cu electron transfer processes, which produce highly active ORR catalytic sites. This work provides not only a new path to engineer a low-cost and efficient replacement for Pt/C for oxygen catalysis but also unveils the underlying details of the ORR mechanism on bimetallic organic frameworks.

METHODS

Chemicals. Copper chloride tetrahydrate and cobalt chloride (99.99% AR, grade) were purchased from Sigma-Aldrich, and benzene-1,3,5-tricarboxylic acid, 1,2,4,5-tetraaminobenzene tetrahydrochloride (BTA), Nafion solution (5 weight%), and sodium hydroxide (NaOH 99.98%) were purchased from Sigma-Aldrich. *N, N*-dimethylformamide (DMF) was bought from Fisher Scientific. All compounds and chemicals were used directly without further purification. Ultrapure distilled water used in the measurements was obtained from a Millipore System (Millipore Q).

Synthesis of the Bimetallic MOFs. DMF (15 mL), ethanol (1 mL), and distilled water (5 mL) were mixed in a 100 mL thin cylindrical tube; 0.5 mmol of BTA and BTC was added to the solution under ultrasonication. Subsequently, 0.2 mmol of CoCl₂ and the same amount of CuCl₂·6H₂O were added. The solution was then magnetically stirred for 10 min to obtain a uniform colloidal suspension. Afterward, the colloidal suspension was continuously ultrasonicated for 10 h. Finally, the mixture was transferred into a 45 mL Teflon vessel at 160 °C for 24 h in an airtight environment. The material was then separated and cleaned in an acidic solution to remove extra unreacted oxides. ^{39–41}

Density Functional Calculations. For a novel CoCuBTABTC MOF structure, it was essential to build the molecular structure of the material of its building blocks which are formed by 1,3,5- benzene tricarboxylic acid (BTC), 1,2,4,5-benzenetetramine (BTA), cobalt metal (Co), and copper metal (Cu). 42-44 Initially, experimental X-ray diffraction pattern (XRD) was used to disclose the unit cell of the crystal structure by the reflex plus code as implemented in the materials studio 7.0 software. Then thermogravimetric (TGA) and FTIR analysis were employed to sketch the molecular structure and identify bonding environment of the MOF material. Finally, the geometry optimization calculations were performed on the modeled

structure using (DMol3)^{43,45} via Local density approximation (LDA) within the exchange correlation Vosko, Wilk, and Nusair (VWN)⁴⁶ based on the double-numeric-polarized (DNP) basis. For the free energy calculation, we used the molecule structure of the proposed MOF, and the geometry optimization calculation were performed by using the B3LYP functional. A local basis cutoff of 4.5 Å with k-points grid of $1 \times 1 \times 1$ was used. The geometry optimization convergence thresholds for energy change, force, and displacement between optimization cycles were set to be 1×10^{-5} Ha, 2×10^{-3} Ha/Å, and 0.005 Å, respectively. The SCF tolerance was set to 1.0×10^{-6} eV/ atom, and the smearing for the orbital occupancy was set to be 0.05 Ha.

Characterization. The Powder X-ray diffraction study was conducted using an irradiation source ($\lambda = 1.54056 \text{ Å}$) at a low scanning speed of 0.1° per min. 47 Pawley refinements were performed over the θ range 5° to 90°, thus refining the unit-cell parameters, the zero point, and background terms using a pseudo-Voigt profile function and a Berar-Baldinozzi asymmetry correction function. The nitrogen adsorption-desorption isotherm was obtained at 77 K using a Micromeritics 3 Flex instrument. The BTC-Co-O-Cu-BTA MOF sample was degassed at 453 K and 5 Pa for 12 h before the adsorption-desorption analysis was conducted. X-ray photoelectron spectroscopy (XPS) spectra of the MOF were obtained using ThermoFisher scientific ESCALAB 250 with a microfocused monochromatic Al Ka X-ray source (15 kV) and a double-focusing full 180° spherical sector electron analyzer. A joel JEM-1230 Transmission Electron Microscopy with the Gatan Orius SC1000 side mount CCD camera at 120 kV was used for obtaining TEM images of the MOF. 48 An X-ray photoelectron spectroscopy (XPS) was conducted using a Thermo Scientific ESCALAB 250 Xi XPS system in which the analysis chamber pressure was 1.5×10^{-9} mbar and the size of the X-ray spot was 500 μ m. FTIR spectra were recorded in the solid state using a Bruker Tensor 27 in transmittance mode. TGA measurements were conducted under a nitrogen flow at a scan rate of 10 °C/min in a Mettler ToledoTGA/DSC 1 Star System.49

Electrochemical Setup. The oxygen reduction reaction measurements were conducted with a three-electrode system using a rotating disk electrode connected to an electrochemical workstation (CHI660E, CH Instrument). The working electrode was polished using α -Al₂O₃ and washed with DI water and ethanol using an ultrasonic instrument. Typically, 50 μg/cm² of the material ink with nafion was drop-cast onto the working electrode surface and then dried at room temperature. The reference electrode was a AglAgCll KCl standard electrode, and the counter electrode was a carbon graphite rod. All the potentials were adjusted to the RHE potential calculated using the equation

$$E_{RHE} = E_{Ag/AgCl} + (0.197 + 0.059pH)V$$
 (1)

All the potentials in this work were referenced to the RHE. The cyclic voltammetry curves of samples were measured in an $\rm O_2$ -saturated 0.1 M NaOH solution using the same rotating disk electrode at zero rotation speed. Linear sweep voltammetry was performed using a scan rate 2 mV s⁻¹ in 0.1 M NaOH after oxygen purging for 30 min. The cyclic voltammetry and linear sweep voltammetry experiments were measured concurrently to monitor the electrocatalyst's degradation. For chronoamperometric stability tests, a static potential was fixed during the oxygen reduction reaction to determine the stability. The zinc-air battery measurements were performed at room temperature, and a mixture of 5 M NaOH with 0.2 M zinc acetate⁵⁰ was used as the electrolyte, while a polished Zn foil was used as the anode. The air cathode was made by drop-casting the material onto carbon cloth with a loading of 3.0 mg cm⁻². The idea was to allow $\rm O_2$ from the air to reach the Co–Cu MOF catalyst.

ASSOCIATED CONTENT

Supporting Information

The Supporting Information is available free of charge at https://pubs.acs.org/doi/10.1021/jacs.1c01096.

XPS measurements; detailed TGA; BET; ORR; LSV under a nitrogen atmosphere; rotating desk electrode measurements; evaluation of electrochemical surface area (ECSA) and active site density and free energy plots (PDF)

Accession Codes

CCDC 2062666 contains the supplementary crystallographic data for this paper. These data can be obtained free of charge via www.ccdc.cam.ac.uk/data_request/cif, or by emailing data_request@ccdc.cam.ac.uk, or by contacting The Cambridge Crystallographic Data Centre, 12 Union Road, Cambridge CB2 1EZ, UK; fax: +44 1223 336033.

AUTHOR INFORMATION

Corresponding Authors

Alain R. Puente Santiago — Department of Chemistry and Biochemistry, University of Texas at El Paso, El Paso, Texas 79968, United States; orcid.org/0000-0002-8491-3565; Email: arpuentesan@utep.edu

Nageh K. Allam — Energy Materials Laboratory, School of Sciences and Engineering, The American University in Cairo, New Cairo 11835, Egypt; orcid.org/0000-0001-9458-3507; Email: nageh.allam@aucegypt.edu

Luis Echegoyen — Department of Chemistry and
Biochemistry, University of Texas at El Paso, El Paso, Texas
79968, United States; ○ orcid.org/0000-0003-1107-9423;
Email: echegoyen@utep.edu

Authors

Mohamed Fathi Sanad — Department of Chemistry and Biochemistry and Department of Environmental Sciences and Engineering, University of Texas at El Paso, El Paso, Texas 79968, United States

Sarah A. Tolba — Energy Materials Laboratory, School of Sciences and Engineering, The American University in Cairo, New Cairo 11835, Egypt

Md Ariful Ahsan — Department of Chemistry and Biochemistry, University of Texas at El Paso, El Paso, Texas 79968, United States; orcid.org/0000-0002-2024-8690

Olivia Fernandez-Delgado — Department of Chemistry and Biochemistry, University of Texas at El Paso, El Paso, Texas 79968, United States; Occid.org/0000-0002-6641-026X

Mina Shawky Adly — Department of Chemistry, Virginia Commonwealth University, Richmond, Virginia 23284—2006, United States; Department of Chemistry, Faculty of Science, Mansoura University, Al-Mansoura 35516, Egypt

Elhussein M. Hashem — FabLab, Centre for Emerging Learning Technologies (CELT), The British University in Egypt (BUE), Elshrouk City, Cairo, Egypt; orcid.org/ 0000-0001-7656-2358

Mohamed Mahrous Abodouh — Energy Materials Laboratory, School of Sciences and Engineering, The American University in Cairo, New Cairo 11835, Egypt

M. Samy El-Shall — Department of Chemistry, Virginia Commonwealth University, Richmond, Virginia 23284—2006, United States; orcid.org/0000-0002-1013-4948

Sreeprasad T. Sreenivasan — Department of Chemistry and Biochemistry, University of Texas at El Paso, El Paso, Texas 79968, United States; Occid.org/0000-0002-5728-0512

Complete contact information is available at:

https://pubs.acs.org/10.1021/jacs.1c01096

Author Contributions

^ΔThese authors contribute equally to the work.

Notes

The authors declare no competing financial interest.

ACKNOWLEDGMENTS

L.E. wants to thank the NSF for the generous support of this work under CHE-1801317. The Robert A. Welch Foundation is also gratefully acknowledged for an endowed chair to L.E. (grant AH-0033). N.K.A. acknowledges the financial support from the Arab-German Young Academy of Sciences and Humanities (AGYA). S.T.S. acknowledges the financial support from UTEP start-up grant, UT STARs award, UTEP-URI award, and the US National Science Foundation (NSF) PREM grant #DMR-1827745. The authors also acknowledge the XRD facilities of the Department of Chemistry at UTEP supported by the Department of Defense (grant No. 64705CHREP).

REFERENCES

- (1) Huang, H.; Zhao, Y.; Bai, Y.; Li, F.; Zhang, Y.; Chen, Y. Conductive Metal—Organic Frameworks with Extra Metallic Sites as an Efficient Electrocatalyst for the Hydrogen Evolution Reaction. *Adv. Sci.* **2020**, *7* (9), 2000012.
- (2) Gong, M.; Cao, Z.; Liu, W.; Nichols, E. M.; Smith, P. T.; Derrick, J. S.; Liu, Y. S.; Liu, J.; Wen, X.; Chang, C. J. Supramolecular Porphyrin Cages Assembled at Molecular-Materials Interfaces for Electrocatalytic CO Reduction. *ACS Cent. Sci.* **2017**, 3 (9), 1032–1040.
- (3) Wang, Q.; Astruc, D. State of the Art and Prospects in Metal—Organic Framework (MOF)-Based and MOF-Derived Nanocatalysis. *Chem. Rev.* **2020**, *120* (2), 1438–1511.
- (4) Li, P.; Jin, Z.; Qian, Y.; Fang, Z.; Xiao, D.; Yu, G. Supramolecular confinement of single Cu atoms in hydrogel frameworks for oxygen reduction electrocatalysis with high atom utilization. *Mater. Today* **2020**, *35*, 78–86.
- (5) Shinde, S. S.; Lee, C. H.; Jung, J.-Y.; Wagh, N. K.; Kim, S.-H.; Kim, D.-H.; Lin, C.; Lee, S. U.; Lee, J.-H. Unveiling dual-linkage 3D hexaiminobenzene metal—organic frameworks towards long-lasting advanced reversible Zn—air batteries. *Energy Environ. Sci.* **2019**, *12* (2), 727–738.
- (6) Wang, W.; Xu, X.; Zhou, W.; Shao, Z. Recent Progress in Metal-Organic Frameworks for Applications in Electrocatalytic and Photocatalytic Water Splitting. *Adv. Sci.* **2017**, *4* (4), 1600371.
- (7) Dou, S.; Li, X.; Wang, X. Rational Design of Metal—Organic Frameworks towards Efficient Electrocatalysis. *ACS Mater. Lett.* **2020**, 2 (9), 1251–1267.
- (8) Wu, H. B.; Lou, X. W. Metal-organic frameworks and their derived materials for electrochemical energy storage and conversion: Promises and challenges. *Sci. Adv.* **2017**, *3* (12), eaap9252.
- (9) Cheng, W.; Zhao, X.; Su, H.; Tang, F.; Che, W.; Zhang, H.; Liu, Q. Lattice-strained metal—organic-framework arrays for bifunctional oxygen electrocatalysis. *Nat. Energy* **2019**, *4* (2), 115–122.
- (10) Xia, B. Y.; Yan, Y.; Li, N.; Wu, H. B.; Lou, X. W.; Wang, X. A metal—organic framework-derived bifunctional oxygen electrocatalyst. *Nat. Energy* **2016**, *1* (1), 15006.
- (11) Voiry, D.; Shin, H. S.; Loh, K. P.; Chhowalla, M. Low-dimensional catalysts for hydrogen evolution and CO2 reduction. *Nat. Rev. Chem.* **2018**, 2 (1), 0105.
- (12) Kuznetsov, D. A.; Han, B.; Yu, Y.; Rao, R. R.; Hwang, J.; Román-Leshkov, Y.; Shao-Horn, Y. Tuning Redox Transitions via Inductive Effect in Metal Oxides and Complexes, and Implications in Oxygen Electrocatalysis. *Joule* **2018**, 2 (2), 225–244.

- (13) Zhang, X.; Luo, J.; Wan, K.; Plessers, D.; Sels, B.; Song, J.; Chen, L.; Zhang, T.; Tang, P.; Morante, J. R.; Arbiol, J.; Fransaer, J. From rational design of a new bimetallic MOF family with tunable linkers to OER catalysts. *J. Mater. Chem. A* **2019**, 7 (4), 1616–1628.
- (14) Zhao, X.; Pattengale, B.; Fan, D.; Zou, Z.; Zhao, Y.; Du, J.; Huang, J.; Xu, C. Mixed-Node Metal—Organic Frameworks as Efficient Electrocatalysts for Oxygen Evolution Reaction. *ACS Energy Lett.* **2018**, 3 (10), 2520–2526.
- (15) Tian, F.; Qiao, C.; Zheng, R.; Ru, Q.; Sun, X.; Zhang, Y.; Meng, C. Synthesis of bimetallic-organic framework Cu/Co-BTC and the improved performance of thiophene adsorption. *RSC Adv.* **2019**, 9 (27), 15642–15647.
- (16) da Silva, G. G.; Machado, F. L. A.; Junior, S. A.; Padrón-Hernández, E. Metal-organic framework: Structure and magnetic properties of [Cu3(BTC)2 (L)x·(CuO)y]n (L = H2O, DMF). *J. Solid State Chem.* **2017**, 253, 1–5.
- (17) Lemkul, J. From proteins to perturbed Hamiltonians: A suite of tutorials for the GROMACS-2018 molecular simulation package [article v1. 0]. *LiveCoMS* **2018**, *1* (1), 5068.
- (18) Yang, S.; Peng, L.; Oveisi, E.; Bulut, S.; Sun, D. T.; Asgari, M.; Trukhina, O.; Queen, W. L. MOF-Derived Cobalt Phosphide/Carbon Nanocubes for Selective Hydrogenation of Nitroarenes to Anilines. *Chem. Eur. J.* **2018**, 24 (17), 4234–4238.
- (19) Liu, W.; Tan, S.; Yang, Z.; Ji, G. Enhanced Low-Frequency Electromagnetic Properties of MOF-Derived Cobalt through Interface Design. ACS Appl. Mater. Interfaces 2018, 10 (37), 31610–31622.
- (20) Lu, W.; Wei, Z.; Gu, Z.-Y.; Liu, T.-F.; Park, J.; Park, J.; Tian, J.; Zhang, M.; Zhang, Q.; Gentle Iii, T. Tuning the structure and function of metal—organic frameworks via linker design. *Chem. Soc. Rev.* **2014**, *43* (16), 5561–5593.
- (21) Rosen, A. S.; Mian, M. R.; Islamoglu, T.; Chen, H.; Farha, O. K.; Notestein, J. M.; Snurr, R. Q. Tuning the Redox Activity of Metal—Organic Frameworks for Enhanced, Selective O2 Binding: Design Rules and Ambient Temperature O2 Chemisorption in a Cobalt—Triazolate Framework. *J. Am. Chem. Soc.* **2020**, *142* (9), 4317—4328.
- (22) Liu, Y.; Liu, S.; Gonçalves, A. A. S.; Jaroniec, M. Effect of metal-ligand ratio on the CO 2 adsorption properties of Cu-BTC metal-organic frameworks. *RSC Adv.* **2018**, 8 (62), 35551–35556.
- (23) Shinozaki, K.; Zack, J. W.; Pylypenko, S.; Pivovar, B. S.; Kocha, S. S. Oxygen reduction reaction measurements on platinum electrocatalysts utilizing rotating disk electrode technique: II. Influence of ink formulation, catalyst layer uniformity and thickness. *J. Electrochem. Soc.* **2015**, *162* (12), F1384.
- (24) Chen, Y.; Cheng, T.; Goddard Iii, W. A. Atomistic Explanation of the Dramatically Improved Oxygen Reduction Reaction of Jagged Platinum Nanowires, 50 times better than Pt. J. Am. Chem. Soc. 2020, 142 (19), 8625–8632.
- (25) Liang, Y.; Li, Y.; Wang, H.; Zhou, J.; Wang, J.; Regier, T.; Dai, H. Co3O4 nanocrystals on graphene as a synergistic catalyst for oxygen reduction reaction. *Nat. Mater.* **2011**, *10* (10), 780–786.
- (26) Campos-Roldán, C. A.; González-Huerta, R. G.; Alonso-Vante, N. Experimental protocol for HOR and ORR in alkaline electrochemical measurements. *J. Electrochem. Soc.* **2018**, *165* (15), J3001.
- (27) Li, J.; Meng, Z.; Brett, D. J. L.; Shearing, P. R.; Skipper, N. T.; Parkin, I. P.; Gadipelli, S. High Performance Zinc-Air Battery with Scalable Metal-Organic Framework and Platinum Carbon Black Bifunctional Catalyst. ACS Appl. Mater. Interfaces 2020, 12 (38), 42696–42703.
- (28) Yuan, Y.; Wang, J.; Adimi, S.; Shen, H.; Thomas, T.; Ma, R.; Attfield, J. P.; Yang, M. Zirconium nitride catalysts surpass platinum for oxygen reduction. *Nat. Mater.* **2020**, *19* (3), 282–286.
- (29) Löhnert, C.; Stürzer, T.; Tegel, M.; Frankovsky, R.; Friederichs, G.; Johrendt, D. Superconductivity up to 35 K in the iron platinum arsenides (CaFe1- xPtxAs) 10Pt4- yAs8 with layered structures. *Angew. Chem., Int. Ed.* **2011**, *50* (39), 9195–9199.
- (30) Zhang, J.; Zhao, Y.; Guo, X.; Chen, C.; Dong, C.-L.; Liu, R.-S.; Han, C.-P.; Li, Y.; Gogotsi, Y.; Wang, G. Single platinum atoms

- immobilized on an MXene as an efficient catalyst for the hydrogen evolution reaction. *Nat. Catal.* **2018**, *1* (12), 985–992.
- (31) Tong, Y.; Zhang, X.-y.; Wang, Q.; Xu, X. The adsorption mechanism of platinum on phosphorus-doped single walled carbon nanotube. *Comput. Theor. Chem.* **2015**, *1059*, 1–6.
- (32) Yuan, Y.; Wang, J.; Adimi, S.; Shen, H.; Thomas, T.; Ma, R.; Attfield, J. P.; Yang, M. Zirconium nitride catalysts surpass platinum for oxygen reduction. *Nat. Mater.* **2020**, *19* (3), 282–286.
- (33) Li, L.; He, J.; Wang, Y.; Lv, X.; Gu, X.; Dai, P.; Liu, D.; Zhao, X. Metal—organic frameworks: a promising platform for constructing non-noble electrocatalysts for the oxygen-reduction reaction. *J. Mater. Chem. A* **2019**, 7 (5), 1964–1988.
- (34) Zhong, L.; Li, S. Unconventional Oxygen Reduction Reaction Mechanism and Scaling Relation on Single-Atom Catalysts. *ACS Catal.* **2020**, *10* (7), 4313–4318.
- (35) Jiao, W.; Chen, C.; You, W.; Chen, G.; Xue, S.; Zhang, J.; Liu, J.; Feng, Y.; Wang, P.; Wang, Y. Tuning strain effect and surface composition in PdAu hollow nanospheres as highly efficient ORR electrocatalysts and SERS substrates. *Appl. Catal., B* **2020**, 262, 118298.
- (36) Zhao, S.; Wang, Y.; Dong, J.; He, C.-T.; Yin, H.; An, P.; Zhao, K.; Zhang, X.; Gao, C.; Zhang, L.; Lv, J.; Wang, J.; Zhang, J.; Khattak, A. M.; Khan, N. A.; Wei, Z.; Zhang, J.; Liu, S.; Zhao, H.; Tang, Z. Ultrathin metal—organic framework nanosheets for electrocatalytic oxygen evolution. *Nat. Energy* **2016**, *1* (12), 16184.
- (37) Suntivich, J.; May, K. J.; Gasteiger, H. A.; Goodenough, J. B.; Shao-Horn, Y. A perovskite oxide optimized for oxygen evolution catalysis from molecular orbital principles. *Science* **2011**, 334 (6061), 1383–1385.
- (38) Yao, Z.; Kim, S.; He, J.; Hegde, V. I.; Wolverton, C. Interplay of cation and anion redox in Li $_4$ Mn $_2$ O $_5$ cathode material and prediction of improved Li $_4$ (Mn,M) $_2$ O $_5$ electrodes for Li-ion batteries. *Sci. Adv.* **2018**, *4* (5), eaao6754.
- (39) Du, J.; Shi, X.; Shan, Y.; Wang, Y.; Zhang, W.; Yu, Y.; Shan, W.; He, H. The effect of crystallite size on low-temperature hydrothermal stability of Cu-SAPO-34. *Catal. Sci. Technol.* **2020**, *10* (9), 2855–2863.
- (40) Shoji, S.; Peng, X.; Yamaguchi, A.; Watanabe, R.; Fukuhara, C.; Cho, Y.; Yamamoto, T.; Matsumura, S.; Yu, M.-W.; Ishii, S. Photocatalytic uphill conversion of natural gas beyond the limitation of thermal reaction systems. *Nat. Catal.* **2020**, *3* (2), 148–153.
- (41) Jiang, Y.; Gao, J.; Zhang, Q.; Liu, Z.; Fu, M.; Wu, J.; Hu, Y.; Ye, D. Enhanced oxygen vacancies to improve ethyl acetate oxidation over MnOx-CeO2 catalyst derived from MOF template. *Chem. Eng. J.* **2019**, *371*, 78–87.
- (42) Eddaoudi, M.; Moler, D. B.; Li, H.; Chen, B.; Reineke, T. M.; O'Keeffe, M.; Yaghi, O. M. Modular chemistry: secondary building units as a basis for the design of highly porous and robust metalorganic carboxylate frameworks. *Acc. Chem. Res.* **2001**, 34 (4), 319–30.
- (43) Delley, B. From molecules to solids with the DMol3 approach. *J. Chem. Phys.* **2000**, *113* (18), 7756–7764.
- (44) Tranchemontagne, D. J.; Mendoza-Cortés, J. L.; O'Keeffe, M.; Yaghi, O. M. Secondary building units, nets and bonding in the chemistry of metal—organic frameworks. *Chem. Soc. Rev.* **2009**, 38 (5), 1257–1283.
- (45) Delley, B. DMol3 DFT studies: from molecules and molecular environments to surfaces and solids. *Comput. Mater. Sci.* **2000**, *17* (2–4), 122–126.
- (46) Vosko, S. H.; Wilk, L. Influence of an improved local-spin-density correlation-energy functional on the cohesive energy of alkali metals. *Phys. Rev. B: Condens. Matter Mater. Phys.* **1980**, 22 (8), 3812.
- (47) Vorobyeva, E.; Gerken, V. C.; Mitchell, S.; Sabadell-Rendón, A.; Hauert, R.; Xi, S.; Borgna, A.; Klose, D.; Collins, S. M.; Midgley, P. A.; Kepaptsoglou, D. M.; Ramasse, Q. M.; Ruiz-Ferrando, A.; Fako, E.; Ortuño, M. A.; López, N.; Carreira, E. M.; Pérez-Ramírez, J. Activation of Copper Species on Carbon Nitride for Enhanced Activity in the Arylation of Amines. *ACS Catal.* **2020**, *10* (19), 11069—11080.

- (48) Murugappan, K.; Anderson, E. M.; Teschner, D.; Jones, T. E.; Skorupska, K.; Román-Leshkov, Y. Operando NAP-XPS unveils differences in MoO 3 and Mo 2 C during hydrodeoxygenation. *Nat. Catal.* **2018**, *1* (12), 960–967.
- (49) Ahsan, M. A.; Puente Santiago, A. R.; Hong, Y.; Zhang, N.; Cano, M.; Rodriguez-Castellon, E.; Echegoyen, L.; Sreenivasan, S. T.; Noveron, J. C. Tuning of Trifunctional NiCu Bimetallic Nanoparticles Confined in a Porous Carbon Network with Surface Composition and Local Structural Distortions for the Electrocatalytic Oxygen Reduction, Oxygen and Hydrogen Evolution Reactions. *J. Am. Chem. Soc.* **2020**, *142* (34), *14688*–14701.
- (50) Bu, Y. F.; Gwon, O.; Nam, G.; Jang, H.; Kim, S.; Zhong, Q.; Cho, J.; Kim, G. A Highly Efficient and Robust Cation Ordered Perovskite Oxide as a Bifunctional Catalyst for Rechargeable Zinc-Air Batteries. ACS Nano 2017, 11 (11), 11594–11601.